No-Reference Image Blur Assessment Based on Discrete Orthogonal Moments

Leida Li, *Member, IEEE*, Weisi Lin, *Senior Member, IEEE*, Xuesong Wang, Gaobo Yang,
Khosro Bahrami, *Student Member, IEEE*, and Alex C. Kot, *Fellow, IEEE*

Abstract—Blur is a key determinant in the perception of image quality. Generally, blur causes spread of edges, which leads to shape changes in images. Discrete orthogonal moments have been widely studied as effective shape descriptors. Intuitively, blur can be represented using discrete moments since noticeable blur affects the magnitudes of moments of an image. With this consideration, this paper presents a blind image blur evaluation algorithm based on discrete Tchebichef moments. The gradient of a blurred image is first computed to account for the shape, which is more effective for blur representation. Then the gradient image is divided into equal-size blocks and the Tchebichef moments are calculated to characterize image shape. The energy of a block is computed as the sum of squared non-DC moment values. Finally, the proposed image blur score is defined as the variance-normalized moment energy, which is computed with the guidance of a visual saliency model to adapt to the characteristic of human visual system. The performance of the proposed method is evaluated on four public image quality databases. The experimental results demonstrate that our method can produce blur scores highly consistent with subjective evaluations. It also outperforms the state-of-the-art image blur metrics and several general-purpose no-reference quality metrics.

Index Terms—Blur, image quality assessment (IQA), no-reference (NR), Tchebichef moments, visual saliency.

I. INTRODUCTION

DIGITAL images are inevitably subject to various kinds of distortions during their acquisition and processing. Objective image quality assessment (IQA) metrics build computational models to evaluate the quality of images, and meantime maintain consistency with subjective evaluations [1]. IQA metrics are essential for benchmarking image processing algorithms, such as image denoising, deblurring, superresolution, and watermarking [2]–[5]. They can also be used for

online quality monitoring and parameter optimization of image processing algorithms.

According to the availability of a reference image, the current IQA algorithms can be classified into full-reference (FR), reduced-reference (RR), and no-reference (NR) metrics [6]. FR metrics employ both the distorted image and the corresponding undistorted reference image to generate the quality score [7]–[12]. In RR metrics, partial information is extracted using feature extraction methods, and then transmitted to the receiver side for quality assessment [13]–[15]. The requirement of full/partial information of the reference image is a drawback of FR/RR-IQA metrics. By comparison, NR or blind metrics can evaluate image quality using the distorted image directly. Therefore, blind IQA metrics potentially have more applications in real-world scenarios [16]. Blind IQA metrics can be further classified into distortion-specific and general-purpose approaches. In distortion-specific metrics, one type of distortion is evaluated, such as blocking artifacts, blur, and ringing effects [17]–[19]. In general-purpose metrics, image quality is evaluated without knowing the exact distortion types [20]–[28].

In this paper, we focus on blind assessment of blur in images using discrete orthogonal moments. Discrete moments have been shown effective in shape description [29]–[32]. Image blur is mainly characterized by the spread of edges. When an image is blurred, the spread edges cause shape change of the image, and this kind of shape change can be captured by discrete moments. Based on this observation, this paper presents a blind image blur evaluation (BIBLE) algorithm using Tchebichef moments. The gradient of a blurred image is first computed to denote the shape, which is more effective for blur representation. Then the gradient image is divided into equal-size blocks and the Tchebichef moments are computed. The energy of a block is calculated using the sum of squared non-DC moment (SSM) values. Then image blur score is defined as the variance-normalized moment energy, which is computed with the guidance of a visual saliency model to adapt to the characteristic of the human visual system (HVS). We test the performance of the proposed method on four public subjectively-rated image quality databases. The experimental results demonstrate the advantages of the proposed method.

II. RELATED WORK

Blur is a key determinant in the perception of image quality. During the past few years, several algorithms have

been proposed for image blur assessment. These metrics can be classified into spatial-domain and transform-domain approaches. Marziliano *et al.* [33] first detected image edges using the Sobel operator. Then the spread of edges was measured by the widths of the edges, and image blur score was defined as the average edge width. Wu *et al.* [34] measured image blur using the point spread function (PSF). The PSF was computed based on the line spread function, which was also constructed from image edges. Ferzli and Karam [35] proposed the just noticeable blur (JNB) metric. Image blur was represented by a probability summation model, which was computed based on local contrast and edge width. An extension of the JNB metric was also proposed by computing the cumulative probability of blur detection (CPBD) [36]. Bahrami and Kot [37] proposed a method based on the maximum local variation (MLV). The MLV of a pixel was first computed within its 8-pixel neighborhood. Then the MLVs were weighted based on their rankings. Finally, the standard deviation of the weighted MLV distribution was computed as the blur score. Among the transform-domain approaches, Vu and Chandler [38] addressed a method in the wavelet domain. A blurred image was first decomposed by a three-level discrete wavelet transform (DWT). Then a weighted average of the log-energies of the DWT coefficients was used as the blur score. Hassen *et al.* [39] proposed a novel method based on local phase coherence (LPC), which was computed in the complex wavelet domain. It was based on the fact that image blur disrupted the LPC structure, and the strength of LPC could be used to measure the extent of blur. In [40], a hybrid-domain approach was addressed. The slope of local magnitude spectrum was used to measure the attenuation of high-frequency content, and total variation was used to account for local contrast. A combination of these two factors was proved effective for image blur assessment.

It has been widely accepted that structures are important for IQA [7]. Typically, image structures are present in the form of edge and gradient. Orthogonal moments have been shown effective in capturing edge features in digital images [41], [42]. Recently, attempts have been done to use orthogonal moments for IQA. Wee *et al.* [43] proposed a FR-IQA metric based on discrete orthogonal moments. Both reference and distorted images were divided into blocks, and discrete moments were employed to measure the similarity of the blocks. The quality score was defined as the average block similarity. An improved version of this method was also proposed by classifying the blocks into three types (plain, edge, and texture) and assigning different weights when computing the quality score [44]. More recently, Li *et al.* [17] proposed a Tchebichef-moment-based NR metric for evaluating blocking artifacts in JPEG images. High-odd-order moments were employed to characterize the abrupt changes around the block boundaries, which were caused by blocking artifacts. To the best of our knowledge, the current moment-based IQA metrics are confined to FR approaches and NR blocking artifacts assessment, and little work has been done to use orthogonal moments for image blur assessment.

TABLE I
NOTATIONS USED IN THIS PAPER

Symbol	Meaning	Symbol	Meaning
$\mathbf{I}$	Image	$\mathbf{G}$	Gradient image
$M \times N$	Image size	$\mathbf{B}_{ij}^{I}$	Image block
$D \times D$	Block size	σ_{ij}^2	Image block variance
$\mathbf{B}_{ij}^{G}$	Gradient block	$P \times Q$	Number of blocks
$t_n(x; N)$	Tchebichef kernel	$\tilde{t}_n(x; N)$	Weighted Tchebichef kernel
$w(x; N)$	Weight	$\rho(n; N)$	Norm
T_{mn}	$(m+n)$th order moment	$\mathbf{K}_1, \mathbf{K}_2$	Tchebichef kernel matrix
E_{ij}	Non-DC moment energy	S	Normalized image energy
$\mathbf{W}$	Saliency map	$\widetilde{\mathbf{W}}$	Resized saliency map
S_{BIBLE}	Blur score		

III. DISCRETE TCHEBICHEF MOMENTS

Tchebichef, Krawtchouk, and Hahn moments are the three kinds of discrete orthogonal moments that are commonly used in the literatures [30]–[32]. Tchebichef moments are global shape descriptors, and they extract features from the whole image. By contrast, Krawtchouk and Hahn moments are local descriptors, since they are computed with emphasis on a specific region of an image. In this paper, we aim to measure blur of a whole image, so Tchebichef moments are preferred. In this section, we briefly introduce Tchebichef moments and analyze their properties. For clarity, the notations used in this paper are listed in Table I, which will be useful later.

A. Definition

As shape descriptors, Tchebichef moments have been found effective in image analysis due to their superior capabilities of feature representation. Unlike the well-known Zernike moments, Tchebichef moments are defined directly on image coordinates, so there is no approximation error in the computation of Tchebichef moments. The computation of discrete Tchebichef moments is to project an image onto a set of weighted Tchebichef kernels.

The nth order, N-point weighted Tchebichef kernel is defined as [30], [32]

$$\tilde{t}_n(x; N) = \sqrt{\frac{w(x; N)}{\rho(n; N)}} t_n(x; N) \tag{1}$$

where $w(x; N) = \frac{1}{N+1}$ and $\rho(n; N) = \frac{(2n)!}{N+1}\binom{N+n+1}{2n+1}$ are the weight and norm used to ensure numerical stability [30]; $t_n(x; N)$ is the Tchebichef kernel

$$t_n(x; N) = n! \sum_{k=0}^{n} (-1)^{n-k} \binom{N-1-k}{n-k} \binom{n+k}{n} \binom{x}{k}. \tag{2}$$

These weighted kernels satisfy the following orthonormal condition:

$$\sum_{x=0}^{N-1} \tilde{t}_m(x; N)\tilde{t}_n(x; N) = \delta_{mn} \tag{3}$$

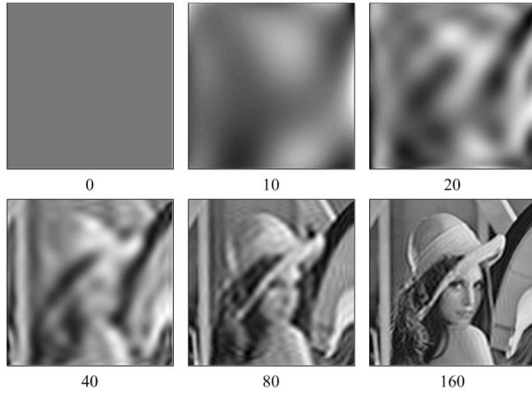where δ_{mn} is the Kronecker delta. More computational issues of Tchebichef kernels can be found in [45].

Fig. 1. Reconstructed images of the original image *Lena* (128×128) using Tchebichef moments up to different maximum orders.

Fig. 2. Three blurred images and their gradient images. The gradient images are converted to the range [0, 255] for display. (a)-(c) Blurred images. (d)-(f) Corresponding gradient images.

With the weighted Tchebichef kernels, the $(m+n)$th order Tchebichef moments of an $M \times N$ image $f(x, y)$ is defined as

$$T_{mn} = \sum_{x=0}^{M-1} \sum_{y=0}^{N-1} \tilde{t}_m(x; M)\tilde{t}_n(y; N)f(x, y) \qquad (4)$$

where $m \in \{0, 1, 2, \ldots, M-1\}$, $n \in \{0, 1, 2, \ldots, N-1\}$.

In implementation, the Tchebichef moments up to the $(m+n)$th order can be computed by matrix multiplications

$$\mathbf{T} = \mathbf{K}_1 \mathbf{I} \mathbf{K}_2' \qquad (5)$$

where $\mathbf{I}$ is an image and $\mathbf{K}_2'$ denotes the transpose of $\mathbf{K}_2$. $\mathbf{K}_1$ and $\mathbf{K}_2$ are kernel matrices defined as follows:

$$\mathbf{K}_1 = \left\{\tilde{t}_i(j; M)\right\}_{i,j=0}^{i=m,j=M-1}, \mathbf{K}_2 = \left\{\tilde{t}_i(j; N)\right\}_{i,j=0}^{i=n,j=N-1}. \quad (6)$$

The weighted Tchebichef kernels constitute a complete and orthogonal set, so the image can be fully characterized by the total $M \times N$ moments. Therefore, an image can be reconstructed using the Tchebichef moments as follows:

$$f(x, y) = \sum_{m=0}^{M-1} \sum_{n=0}^{N-1} \tilde{t}_m(x; M)\tilde{t}_n(y; N)T_{mn}. \qquad (7)$$

In practice, if a subset of Tchebichef moments $\{T_{mn}\}$, $m \in \{0, 1, 2, \ldots, m_{\max}\}$, $n \in \{0, 1, 2, \ldots, n_{\max}\}$, is available, an approximated image $\hat{f}(x, y)$ can be obtained as

$$\hat{f}(x, y) = \sum_{m=0}^{m_{\max}} \sum_{n=0}^{n_{\max}} \tilde{t}_m(x; M)\tilde{t}_n(y; N)T_{mn}. \qquad (8)$$

B. Analysis of Tchebichef Moments

An important property of Tchebichef moments is that the moments with different orders have varying image representation abilities. Specifically, low-order moments capture low-frequency components of an image, and high-order moments capture high-frequency components. Fig. 1 shows an example of the reconstructed versions of an original image *Lena* (128×128) using Tchebichef moments up to different maximum orders.

It is observed from the figure that the reconstructed images become closer to the original image with the increase of
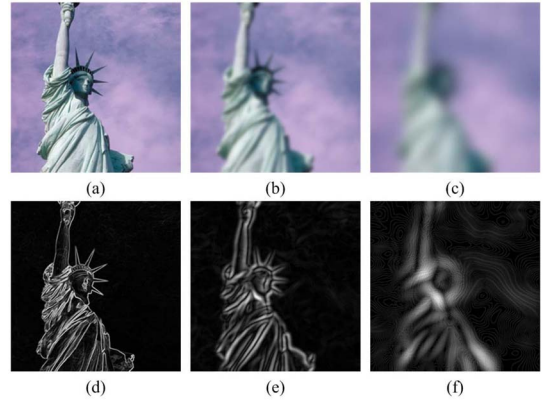
moment order. Low-order reconstructed images mainly contain rough shapes of the image, and high-order reconstructed images contain more fine details. Furthermore, the zero-order reconstructed image is constant. In fact, the zeroth order Tchebichef moment denotes the average value of an image, namely the DC component [30]. Since image blur is characterized by the spread of edges and accordingly attenuation of high-frequency components, it is intuitive that blur has direct impact on the Tchebichef moments, based on which the extent of blur can be estimated.

IV. BIBLE

As effective shape descriptors, Tchebichef moments have been widely used in image analysis [30]. In this paper, we employ Tchebichef moments to evaluate the extent of blur in images. The motivation behind this paper is that blur causes shape changes in images, and we believe this kind of shape change can be effectively represented using Tchebichef moments, based on which image blur can be measured.

A. Relation Between Blur and Tchebichef Moments

Blur causes attenuation of high-frequency components in images, and the magnitudes of Tchebichef moments change accordingly. To have an intuitional understanding of the relation between image blur and Tchebichef moments, an example is given in Fig. 2. The figure shows an image and its two blurred versions, together with their gradient images obtained using (9). The Tchebichef moments of the blurred and gradient images are computed, and the magnitudes of some obtained moments are summarized in Table II.

It can be seen from Fig. 2 that with the increase of blur, image edges become wider. This is more obvious in the structured regions of the image. For example, in the body parts of the sculpture, the blur distortion is more annoying. Furthermore, the spread edges can be better viewed in the gradient domain. By computing the gradients, we easily obtain the shape of the image; and the extent of blur can be better represented using the gradient image.

From Table II, it is observed that the magnitudes of the moments decrease with the increase of blur. This holds for
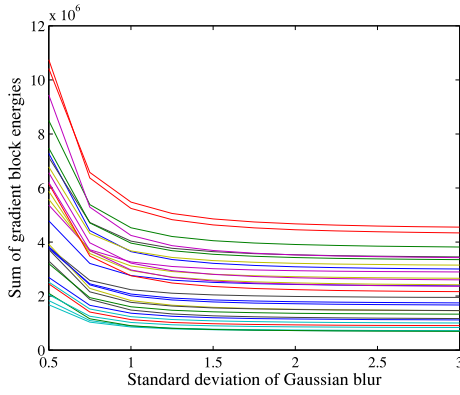
TABLE II
MAGNITUDES OF SOME TCHEBICHEF MOMENTS OF THE BLURRED
AND GRADIENT IMAGES SHOWN IN FIG. 2

Blurred image	T_{10}	T_{13}	T_{23}	T_{35}	T_{42}
(a)	4307.54	2258.00	2777.92	738.67	1465.44
(b)	4305.43	2252.17	2766.20	729.48	1449.29
(c)	4296.90	2177.03	2627.00	634.44	1305.10
Gradient image	T_{10}	T_{13}	T_{23}	T_{35}	T_{42}
(d)	439.84	177.22	310.35	225.60	112.44
(e)	123.18	21.03	67.91	55.54	29.88
(f)	38.67	10.90	35.58	19.53	12.08

Fig. 3. Flowchart of the proposed BIBLE metric.

moments computed from both the blurred and gradient images. The same conclusion has been found after we have tested different images with diversifying visual content. This is not hard to understand, because blur is characterized by the attenuation of high-frequency energy. Another finding is that the decrease of moment magnitudes is not obvious for the blurred images. By contrast, the magnitudes decrease significantly for the gradient images. This indicates that gradient domain is more effective in blur representation than spatial domain. The reason is that in the spatial domain, most of the energy exist in the low-frequency components, which are dominant and stable. By computing the gradients, most of the low-frequency components are removed and high-frequency components become dominant, which are sensitive to blur. As a result, in this paper, we compute the Tchebichef moments using the gradient images instead of the original blurred images.

B. Image Blur Assessment

The flowchart of the proposed method is shown in Fig. 3. It consists of two main stages. In the first stage, we compute the following three components: 1) SSM values for blocks of the gradient image; 2) variances of blocks of the blurred

image; and 3) visual saliency map of the blurred image [47]. The SSM values are used to characterize the image gradient. Block variances are used to conduct a normalization of the SSM values so that we can obtain consistent blur scores across different images. The saliency map is used to adapt to the characteristic of the HVS. In the second stage, these three components are combined to conduct a pooling and the final blur score is computed as the variance-normalized moment energy with the guidance of the saliency map.

In this paper, we evaluate blur from the gradient images, which have been shown more effective for blur representation. For a blurred image in color format, it is first converted into gray scale, which is denoted by $\mathbf{I}(x, y)$, $x \in \{1, 2, 3, \ldots, M\}$, $y \in \{1, 2, 3, \ldots, N\}$. The gradient image is computed as

$$\mathbf{G} = \frac{|\mathbf{G}_x| + |\mathbf{G}_y|}{2} \tag{9}$$

$$\mathbf{G}_x = [-1\ 0\ 1] * \mathbf{I}, \quad \mathbf{G}_y = [-1\ 0\ 1]' * \mathbf{I} \tag{10}$$

where "$'$" denotes the transpose and $*$ is the convolution.

Next, both the gray-scale image and the gradient image are divided into blocks with equal-size $D \times D$. The image block set is denoted by $\{\mathbf{B}_{ij}^I\}$ and the gradient block set is denoted by $\{\mathbf{B}_{ij}^G\}$, $i \in \{1, 2, 3, \ldots, P\}$, $j \in \{1, 2, 3, \ldots, Q\}$, where $P = \lfloor M/D \rfloor$, $Q = \lfloor N/D \rfloor$, and $\lfloor \cdot \rfloor$ is the floor operator. Then the variances of the blocks in $\{\mathbf{B}_{ij}^I\}$ are computed and denoted by $\{\sigma_{ij}^2\}$. The Tchebichef moments of the gradient blocks in $\{\mathbf{B}_{ij}^G\}$ are computed and denoted by $\{\mathbf{T}_{ij}\}$

$$\mathbf{T}_{ij} = \begin{pmatrix} T_{00} & T_{01} & \cdots & T_{0n} \\ T_{10} & T_{11} & \cdots & T_{1n} \\ \vdots & \vdots & \ddots & \vdots \\ T_{m0} & T_{m1} & \cdots & T_{mn} \end{pmatrix} \tag{11}$$

where $m, n \in \{0, 1, 2, \ldots, (D-1)\}$. Then the SSM values (SSM), namely energy of ac moment values, is computed and denoted by $\{E_{ij}\}$

$$E_{ij} = \sum_{p=0}^{m} \sum_{q=0}^{n} (T_{pq})^2 - (T_{00})^2. \tag{12}$$

In (12), $(T_{00})^2$ is removed, because the zeroth order moment denotes the dc component of the image, and we measure the energies of edges and shapes, which are mainly ac components.

It is intuitive that if an image is blurred, the energy of the blurred image will decrease accordingly. In order to demonstrate this, we conduct an experiment on 29 undistorted reference images from the Laboratory for Image and Video Engineering (LIVE) database [49]. Specifically, the images are iteratively filtered using Gaussian low-pass filters with increasing standard derivations. Then the block energies are computed using (12). The relation between the sum of block energies and standard deviation of the Gaussian low-pass filter is shown in Fig. 4.

It is known from the figure that the energy of a blurred image decreases monotonically with the increase of blur strength, i.e., standard deviation of the Gaussian filter. Besides, when an image is severely blurred, the energy tends to

Fig. 4. Relationship between sum of block energies and Gaussian blur standard deviation.

Fig. 5. Image with sharp foreground and blurred background, together with the saliency map detected using SDSP [47]. (a) Sharp image. (b) Saliency map.

approach a constant value; and further blurring has little effect on the image. This also indicates that heavy low-pass filtering can remove most of the high-frequency components and the remaining low-frequency components are relatively stable. From this perspective, the sum of block energies can measure the extent of blur within a single image.

By comparing the curves in Fig. 4, we find that the energies of the blurred images are different even they have the same standard deviation of Gaussian blur. This is easy to understand, because they have completely different contents. Since the standard deviation of Gaussian blur is closely related to subjective score, and we expect to produce similar blur scores for images with similar subjective scores, the effect of image content should be reduced for obtaining objective blur scores across different images.

With the consideration that images with different contents have different variances, we propose to normalize the image energy using the sum of block variances. In this way, we can generate blur scores less sensitive to image content. It should be noted that the variances should be computed on the blocks from the gray-scale image so that they reflect the characteristics of the blurred image. Here, the block variances are denoted by $\{\sigma_{ij}^2\}$, $i \in \{1, 2, 3, \ldots, P\}$, $j \in \{1, 2, 3, \ldots, Q\}$. The normalized image energy is computed as follows:

$$S = \frac{\sum_{i=1}^{P} \sum_{j=1}^{Q} E_{ij}}{\sum_{i=1}^{P} \sum_{j=1}^{Q} \sigma_{ij}^2}. \tag{13}$$

In practice, humans tend to judge the sharpness of an image according to the visually salient regions. Therefore, it is meaningful to incorporate this characteristic to produce the blur score. One such example is shown in Fig. 5(a). The image has sharp foreground and very blurred background. In spite of blurred background, we tend to classify it as a sharp image, because the visually salient regions are sharp. In fact, some of the existing metrics make use of this characteristic to generate the blur score. In [34], the blur score was estimated from the sharpest edges in an image. Vu and Chandler [38] and Vu *et al.* [40] adopted 1% of the largest values in a sharpness map to produce the blur score. Although enhanced results were obtained in these metrics, the parameters were usually determined by experiments. In this paper, we address the problem in a more systematic way by incorporating visual saliency [46].

Fig. 5(b) shows the saliency map detected from Fig. 5(a) using the Saliency Detection by Simple Priors (SDSP) model [47]. It is observed that the detected salient region corresponds to the foreground region, which contributes more in the perception of blur. With the saliency map, the blur score can be generated by assigning bigger weights to the salient regions. As a result, we incorporate visual saliency to generate the overall image blur score.

In this paper, the saliency map of a blurred image is computed and denoted by $\mathbf{W} = \{W_{ij}\}$, $i \in \{1, 2, 3, \ldots, M\}$, $j \in \{1, 2, 3, \ldots, N\}$. Then it is resized to the size $P \times Q$, so that one block corresponds to one weight in the saliency map. Let the resized saliency map be denoted by $\widetilde{\mathbf{W}} = \{\widetilde{W}_{ij}\}$, $i \in \{1, 2, 3, \ldots, P\}, j \in \{1, 2, 3, \ldots, Q\}$, the final image blur score is defined as

$$S_{\text{BIBLE}} = \frac{\sum_{i=1}^{P} \sum_{j=1}^{Q} \widetilde{W}_{ij} \cdot E_{ij}}{\sum_{i=1}^{P} \sum_{j=1}^{Q} \widetilde{W}_{ij} \cdot \sigma_{ij}^2}. \tag{14}$$

For sharp images, the proposed method will generate high blur scores. For blurred images, low scores will be produced.

V. EXPERIMENTAL RESULTS AND DISCUSSION

A. Experimental Settings

The performance of the proposed method is evaluated on four public image quality databases, including LIVE [49], Categorical Subjective Image Quality (CSIQ) [9], Tampere Image Database 2008 (TID2008) [50], and Tampere Image Database 2013 (TID2013) [51]. The blurred images in these databases are obtained using Gaussian low-pass filtering. The numbers of blurred images are 145, 150, 100, and 125, respectively, in the four databases. The subjective qualities of the images in LIVE and CSIQ are measured using difference mean opinion score (DMOS), and in TID2008 and TID2013 mean opinion score (MOS) is used.

Three criterions are used to evaluate the performance, including Pearson linear correlation coefficient (PLCC), Spearman rank order correlation coefficient (SRCC), and root mean square error (RMSE) [52], [53]. PLCC and RMSE are used to measure the prediction accuracy, and SRCC is used to evaluate the prediction monotonicity. To compute these values, a four-parameter logistic fitting is conducted between the subjective and predicted scores [52]

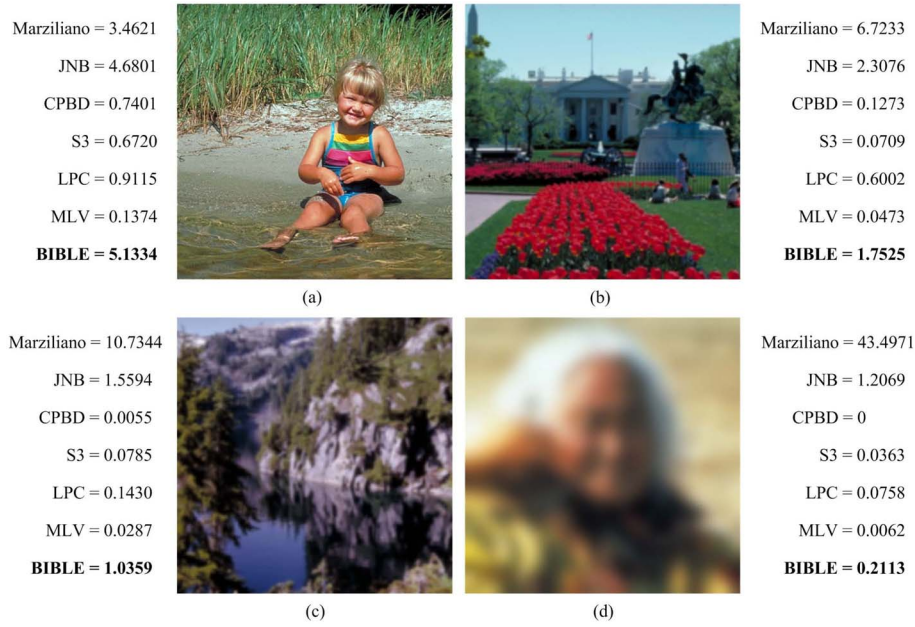$$f(x) = \frac{\tau_1 - \tau_2}{1 + e^{(x - \tau_3)/\tau_4}} + \tau_2 \tag{15}$$

Marziliano = 3.4621

JNB = 4.6801

CPBD = 0.7401

S3 = 0.6720

LPC = 0.9115

MLV = 0.1374

BIBLE = 5.1334

(a)

Marziliano = 6.7233

JNB = 2.3076

CPBD = 0.1273

S3 = 0.0709

LPC = 0.6002

MLV = 0.0473

BIBLE = 1.7525

(b)

Marziliano = 10.7344

JNB = 1.5594

CPBD = 0.0055

S3 = 0.0785

LPC = 0.1430

MLV = 0.0287

BIBLE = 1.0359

(c)

Marziliano = 43.4971

JNB = 1.2069

CPBD = 0

S3 = 0.0363

LPC = 0.0758

MLV = 0.0062

BIBLE = 0.2113

(d)

Fig. 6. Four images with different extents of blur and the predicted scores obtained by different metrics. (a) DMOS = 0.0320. (b) DMOS = 0.4710. (c) DMOS = 0.6550. (d) DMOS = 0.8680.

where $\tau_1, \tau_2, \tau_3,$ and τ_4 are the parameters to be fitted. Generally, a good metric produces high PLCC and SRCC values, as well as a low RMSE value.

In implementation, the size of block is 8×8, and the maximum order of moment is set to 14. These parameters are determined by experiments. For saliency detection, we adopt a recent model SDSP [47], which is fast to compute and has been shown effective for IQA [48].

B. Results and Analysis

1) Image-Level Evaluation: In order to show how the proposed method performs on real images, we test it using several blurred images. Fig. 6 shows four images in the CSIQ database. They have different extents of blur, and the subjective qualities are indicated by the DMOS values. The blur scores generated using the proposed method are given. For comparison, we also provide the scores predicted by six existing blind image blur metrics, namely Marziliano's method [33], JNB [35], CPBD [36], S3 [40], LPC [39], and MLV [37].

It can be seen from the figure that the proposed method can produce blur scores consistent with subjective evaluations. The images shown in Fig. 6 have increasing extents of blur, and our method produces blur scores that decrease monotonically. When compared with the existing methods, we find Marziliano's method [33], JNB, CPBD, LPC, and MLV also produce scores that are consistent with the extents of blur. The S3 metric produces incorrect scores between Fig. 6(b) and (c). As Fig. 6(c) has severer blur than Fig. 6(b), the blur score of Fig. 6(c) is expected to be lower than that of Fig. 6(b). However, S3 produces higher score for Fig. 6(c).

The next experiment is to show how our method performs on images with similar extents of blur. Humans have the capacity to judge the extent of blur independent of image content.

If the images have similar extents of blur, we tend to give similar blur scores. A good blur metric is also expected to have this capacity. In Fig. 7, we show six images with DMOS values in the range (50, 58), which means that their subjective qualities are quite similar. Meantime, from Fig. 7(a)–(f), the DMOS values are monotonically increasing. From this perspective, a good blur metric should produce similar and monotonically decreasing/increasing blur scores. Table III summarizes the blur scores predicted by different metrics.

It is observed from the table that the proposed method can produce similar and monotonically decreasing blur scores for the six images, which are consistent with their subjective scores. By contrast, the blur scores produced by the compared metrics do not satisfy the monotonicity very well. This also indicates that the proposed method can distinguish tiny blur differences between images.

2) Database-Level Evaluation: In this part, we evaluate the overall performance of the proposed method based on the four image quality databases. Fig. 8 shows the scatter plots between the subjective scores provided by the databases and the objective scores predicted by different metrics. For limited space, we only show the results of four recent metrics, i.e., CPBD, S3, LPC, MLV, as well as the proposed BIBLE.

It is observed from the figure that the proposed method achieves very promising results in the four databases. In LIVE, BIBLE, MLV, and S3 produce somewhat similar results, while LPC and CPBD produce slightly worse results. A closer investigation reveals that BIBLE produces the best fitting result and the scatter points are densely clustered around the fitted curve. In CSIQ, BIBLE and MLV produce quite similar fittings, and both fittings are better than those of other metrics. In TID2008 and TID2013, the results produced by BIBLE are better than all the other metrics. Another characteristic that can be seen from the fittings is that the proposed method has the saturation effect. Specifically, for heavily blurred images, the proposed

Fig. 7.   Images with similar extents of blur. Subjective qualities are indicated by the DMOS values below the images. (a) DMOS = 50.7829. (b) DMOS = 52.2833. (c) DMOS = 52.8992. (d) DMOS = 53.6133. (e) DMOS = 54.7958. (f) DMOS = 57.7812.

TABLE III
BLUR SCORES PREDICTED BY DIFFERENT METRICS ON
THE IMAGES SHOWN IN FIG. 7

Image	(a)	(b)	(c)	(d)	(e)	(f)
DMOS	50.7829	52.2833	52.8992	53.6133	54.7958	57.7812
Ref. [33]	5.9404	6.0282	5.4252	5.1228	7.9963	7.1183
JNB [35]	3.0488	2.8476	3.2071	3.2374	1.8879	2.6436
CPBD [36]	0.0637	0.1246	0.3250	0.1531	0.0677	0.0577
S3 [40]	0.0739	0.0791	0.0823	0.0766	0.0657	0.0682
LPC [39]	0.6096	0.7034	0.7413	0.6521	0.5029	0.5086
MLV [37]	0.0575	0.0503	0.0499	0.0335	0.0517	0.0402
BIBLE	2.2723	2.1271	2.0363	2.0008	1.9259	1.9033

method tends to produce similar and low scores. This is consistent with results in Fig. 4, where we have shown that for heavily blurred images the energy tends to approach a constant value. Furthermore, the scatter points are more evenly distributed around the fitted curves for the proposed method. This indicates that our method performs consistently well for both heavily blurred and slightly blurred images.

Table IV summarizes the experimental results of the seven blur metrics on the four databases in terms of PLCC, SRCC, and RMSE. For each database, the best two results are marked in boldface. With the consideration that one metric may have varying performances on different databases, we also compute the weighted average results of the four databases for each metric. Specifically, weighted average is computed by assigning bigger weight to larger database, and the weight is determined by the number of blurred images.

It can be seen from Table IV that the proposed method achieves the best results in LIVE, TID2008, and TID2013 databases, and in CSIQ it ranks the second. In LIVE database, S3 performs the second best, and MLV produces quite similar results with S3. Our metric outperforms the other metrics significantly. In CSIQ database, MLV performs the best. BIBLE is comparable to MLV and it ranks the second. S3 and LPC

achieve quite competitive results, and both outperforms CPBD. The other two metrics do not produce satisfactory results in this database. In TID2008, BIBLE achieves the best results and it significantly outperforms other metrics. Specifically, the PLCC and SRCC values produced by BIBLE are 0.8929 and 0.8915, which are much higher than the second best results, i.e., 0.8584 and 0.8561. In this database, MLV, LPC, and S3 achieve very similar results. In TID2013, BIBLE also produces the best results. LPC ranks the second, followed by MLV. From the average results, we know that the proposed method achieves the best overall performance, in terms of both prediction accuracy and monotonicity.

3) Impact of Block Sizes: In order to investigate the impact of block size on the performance, we have tested different block sizes, ranging from 4×4 to 16×16. For each block size, the highest moment order is used. Table V lists the weighted average results of PLCC and SRCC. It is observed from the table that the performance varies slightly with block sizes, and the best results are obtained when the block size is 8×8. Therefore, we adopt 8×8 blocks in this paper.

4) Impact of Visual Saliency Pooling: In the proposed method, visual saliency is employed to conduct the pooling, which is used to adapt to the characteristics of HVS. Therefore, it is meaningful to investigate the performance of the proposed method without visual saliency pooling. Table VI summarizes the results of BIBLE with/without visual saliency pooling in terms of PLCC and SRCC, together with their weighted average values.

It is observed from the table that, without visual saliency pooling, the proposed method also produces promising results in all databases. By incorporating visual saliency pooling, better results are obtained. While not significant, visual saliency pooling can make the predicted scores more consistent with human scores. This also demonstrates the effectiveness of discrete Tchebichef moments in image blur assessment.
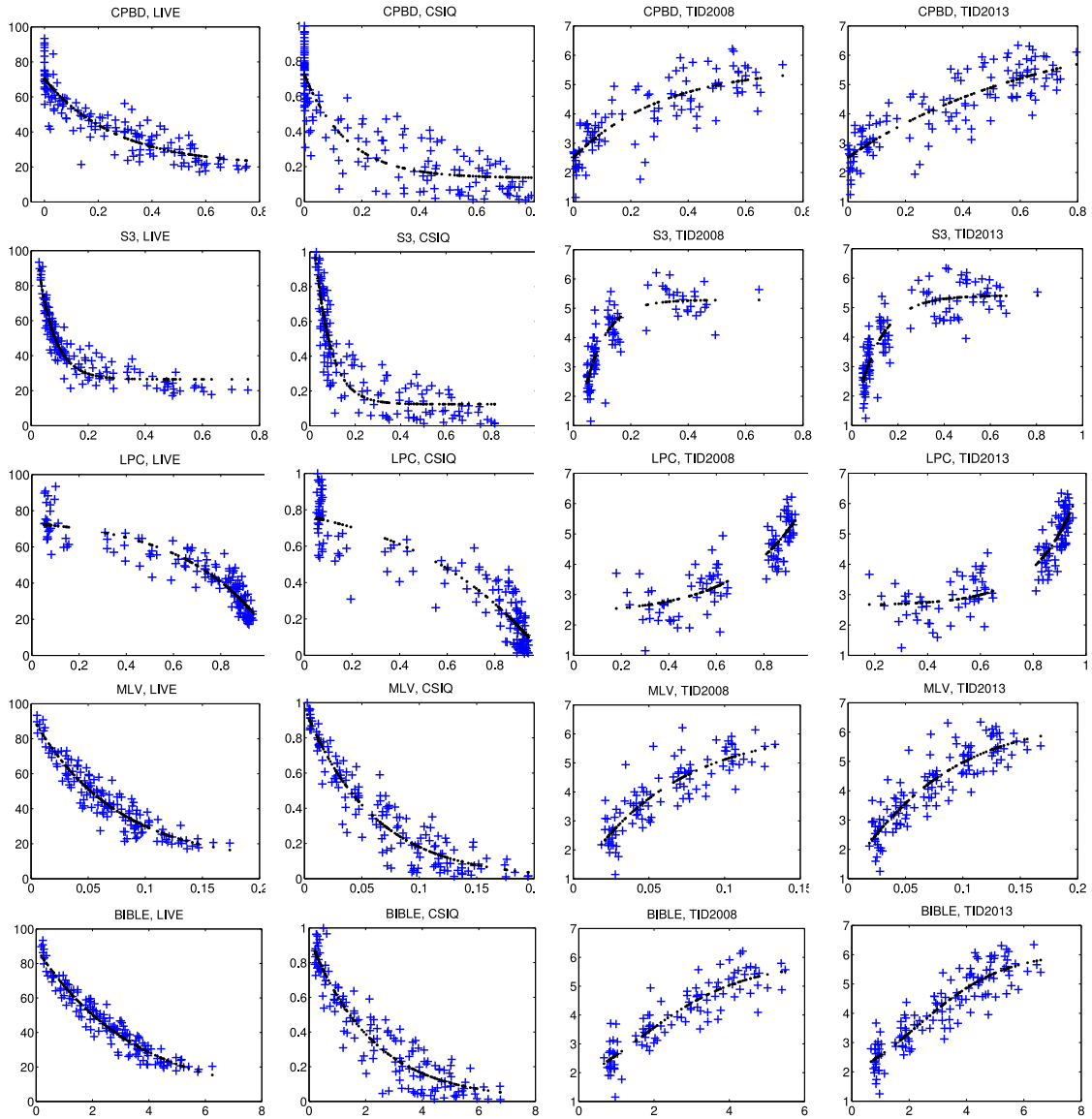
Fig. 8. Scatter plots of the subjective scores versus the predicted blur scores generated by different metrics on four databases. The *x*-axis denotes the metric score, and *y*-axis denotes the subjective score (DMOS for LIVE and CSIQ and MOS for TID2008 and TID2013).

C. Comparison With General-Purpose NR-IQA Metrics

In order to further demonstrate the advantage of the proposed method, we compare BIBLE with the state-of-the-art general-purpose NR-IQA metrics, including blind image quality index (BIQI) [20], blind image integrity notator using DCT statistics (BLIINDS-II) [21], blind/referenceless image spatial quality evaluator (BRISQUE) [22], codebook representation for no-reference image quality assessment (CORNIA) [23], robust BRISQUE (R-BRISQUE) [24], and natural image quality evaluator (NIQE) [25]. In implementation, we use the codes released by the original authors. Table VII summarizes the experimental results, where the two best results are marked in boldface on each database. It should be noted that BIQI, BLIINDS-II, BRISQUE, R-BRISQUE, and CORNIA are learning-based methods, and the images in the LIVE database are used to train a support vector regression model, which is then used to predict the quality scores of other

databases. As a result, their results on the LIVE database are not fair to compare, which are marked by "training on LIVE" in the table [37], [39].

It is observed from the table that, except for CORNIA, the proposed method outperforms other state-of-the-art general-purpose NR-IQA models. Especially in TID2008 and TID2013 databases, CORNIA and BIBLE significantly outperform the other metrics. Although BIBLE does not produce the best results, it performs only slightly worse than CORNIA.

D. Performance on Other Distortions

In this part, we test the proposed method on other distortions. BIBLE is designed for evaluating image blur, which is achieved by measuring the attenuation of high-frequency energy via discrete Tchebichef moments. So, it also works on distortions that may cause attention of high-frequency information in an image. In this experiment, we first test three

TABLE IV
SUMMARY OF EXPERIMENTAL RESULTS FOR THE PROPOSED BIBLE AND SIX EXISTING IMAGE BLUR METRICS

Database	Criterion	Marziliano [33]	JNB [35]	CPBD [36]	S3 [40]	LPC [39]	MLV [37]	BIBLE
LIVE (145 images)	PLCC	0.7980	0.8161	0.8955	**0.9433**	0.9181	0.9429	**0.9622**
	SRCC	0.7977	0.7872	0.9182	**0.9436**	0.9389	0.9312	**0.9607**
	RMSE	11.1317	10.6753	8.2216	**6.1289**	7.3224	6.1522	**5.0320**
CSIQ (150 images)	PLCC	0.7936	0.8061	0.8818	0.9107	0.9158	**0.9488**	0.9403
	SRCC	0.7661	0.7624	0.8853	0.9059	0.9071	**0.9247**	0.9132
	RMSE	0.1744	0.1696	0.1351	0.1184	0.1151	**0.0905**	0.0975
TID2008 (100 images)	PLCC	0.7010	0.6931	0.8235	0.8541	0.8574	0.8584	**0.8929**
	SRCC	0.7042	0.6667	0.8412	0.8418	**0.8561**	0.8548	**0.8915**
	RMSE	0.8369	0.8459	0.6657	0.6103	0.6040	**0.6019**	**0.5284**
TID2013 (125 images)	PLCC	0.7661	0.7113	0.8552	0.8813	**0.8917**	0.8827	**0.9051**
	SRCC	0.7620	0.6902	0.8518	0.8609	**0.8888**	0.8787	**0.8988**
	RMSE	0.8020	0.8771	0.6467	0.5896	**0.5647**	0.5885	**0.5305**
Weighted average	PLCC	0.7704	0.7644	0.8680	0.9018	0.8994	**0.9138**	**0.9288**
	SRCC	0.7620	0.7336	0.8779	0.8933	0.9018	**0.9020**	**0.9188**
	RMSE	3.5081	3.3992	2.6150	2.0023	2.3269	**1.9984**	**1.6604**

TABLE V
WEIGHTED AVERAGE VALUES OF PLCC AND SRCC
WITH DIFFERENT BLOCK SIZES

Size	4×4	6×6	8×8	10×10	12×12	16×16
PLCC	0.9142	0.9249	**0.9288**	0.9250	0.9222	0.9146
SRCC	0.9058	0.9147	**0.9188**	0.9132	0.9064	0.8967

TABLE VI
PLCC AND SRCC RESULTS OF THE PROPOSED METRIC
WITH/WITHOUT VISUAL SALIENCY POOLING

Database	LIVE	CSIQ	TID2008	TID2013	Average
With visual saliency pooling					
PLCC	0.9622	0.9403	0.8929	0.9051	0.9288
SRCC	0.9607	0.9132	0.8915	0.8988	0.9188
Without visual saliency pooling					
PLCC	0.9563	0.9366	0.8860	0.9038	0.9245
SRCC	0.9525	0.9072	0.8853	0.8983	0.9135

TABLE VII
COMPARISON WITH GENERAL-PURPOSE NR-IQA METRICS

Measure	PLCC	SRCC	RMSE	PLCC	SRCC	RMSE
	LIVE			CSIQ		
BIQI [20]	Training on LIVE			0.8556	0.7713	0.1483
BLIINDS-II [21]	Training on LIVE			0.9102	0.8915	0.1187
BRISQUE [22]	Training on LIVE			0.9279	0.9033	0.1068
R-BRISQUE [24]	Training on LIVE			0.9134	0.8861	0.1167
CORNIA [23]	Training on LIVE			**0.9499**	**0.9188**	**0.0895**
NIQE [25]	0.9434	0.9329	6.1278	0.9260	0.8945	0.1082
BIBLE	**0.9622**	**0.9607**	**5.0320**	0.9403	0.9132	0.0975
	TID2008			TID2013		
BIQI [20]	0.7550	0.7468	0.7694	0.7819	0.7642	0.7780
BLIINDS-II [21]	0.8415	0.8388	0.6339	0.8580	0.8557	0.6409
BRISQUE [22]	0.8047	0.7989	0.6967	0.8240	0.8134	0.7070
R-BRISQUE [24]	0.7918	0.8068	0.7168	0.8495	0.8552	0.6583
CORNIA [23]	**0.8902**	**0.9023**	**0.5343**	0.9169	0.9209	0.4978
NIQE [25]	0.8315	0.8165	0.6518	0.8165	0.7968	0.7204
BIBLE	**0.8929**	**0.8915**	**0.5284**	**0.9051**	**0.8988**	**0.5305**

common distortions in the four databases, i.e., JPEG2000 compression, JPEG compression, and added white Gaussian noise (AWGN). Then, we test another four types of distortions that are characterized by attenuation of high-frequency components, including image denoising, sparse sampling and reconstruction, chromatic aberration, and fast fading. Fig. 9 shows intuitively some distortions that cause attenuation of high-frequency components of an image. The simulation results are summarized in Table VIII.

It is known from Table VIII that the proposed method is also effective in evaluating JPEG2000, image denoising, sparse sampling and reconstruction, chromatic aberration, and fast fading. This is because these distortions can all lead to, to some extent, loss of high-frequency components, which can be clearly seen from Fig. 9. Meantime, we also know that the proposed method is not effective in measuring JPEG compression and Gaussian noise. This is due to the fact that BIBLE is achieved by measuring the attenuation of high-frequency energy, but JPEG and AWGN are both characterized by addition of high-frequency components in an image.
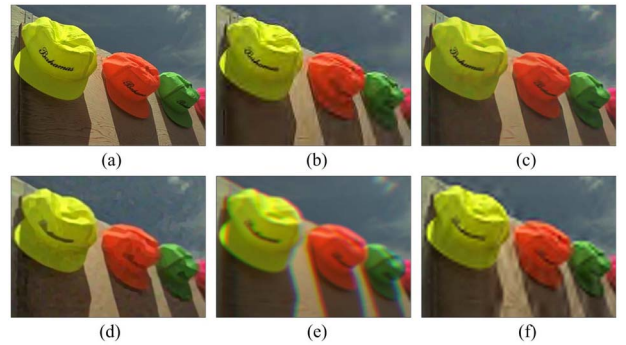

Fig. 9. Distortions that cause attenuation of high-frequency components. (a) Original image. (b) JPEG2000. (c) Image denoising. (d) Sparse sampling and reconstruction. (e) Chromatic aberration. (f) Fast fading.

E. Time Complexity

In order to evaluate the time complexity, we conduct an experiment on the CSIQ database. Specifically, all the NR-IQA metrics are employed to predict the quality scores of the 150 blurred images with size 512×512 in CSIQ database. Then the average computational time is calculated for evaluating the

TABLE IX
AVERAGE COMPUTATIONAL TIME IN GENERATING QUALITY SCORES OF BLURRED IMAGES WITH SIZE 512×512 IN CSIQ DATABASE

Metric	Ref. [33]	JNB	CPBD	S3	LPC	MLV	BIQI	BLIINDS-II	BRISQUE	R-BRISQUE	CORNIA	NIQE	BIBLE
Time (sec)	0.29	0.48	0.54	14.42	0.59	0.07	0.32	44.31	0.15	0.25	2.59	0.18	1.55

TABLE VIII
EXPERIMENTAL RESULTS ON OTHER DISTORTIONS

Distortion	Database	PLCC	SRCC	RMSE
JPEG2000	LIVE	0.8584	0.8458	12.9437
	CSIQ	0.8574	0.8016	0.1626
	TID2008	0.9396	0.9332	0.6680
	TID2013	0.9365	0.9074	0.5973
JPEG	LIVE	0.4572	0.4329	28.3275
	CSIQ	0.5041	0.4601	0.1666
	TID2008	0.7603	0.7317	1.1066
	TID2013	0.8113	0.7750	0.8805
AWGN	LIVE	0.5873	0.4544	22.6440
	CSIQ	0.2943	0.3925	0.1604
	TID2008	0.3320	0.3492	0.5763
	TID2013	0.4394	0.5025	0.6370
Image denoising	TID2008	0.8710	0.8299	0.7871
	TID2013	0.8662	0.7829	0.7822
Sparse sam. & rec.	TID2013	0.9106	0.8749	0.7680
Chromatic aberration	TID2013	0.9531	0.8039	0.4421
Fast fading	LIVE	0.8534	0.8651	14.8472

time complexity of each metric. All tests are conducted on a PC with Intel Core i5 CPU at 3.20 GHz, 8 GB RAM, Windows 7 64-bit, and MATLAB R2012b. Table IX summarizes the experimental results.

It is observed from the table that the proposed method has moderate computational cost. CORNIA is slightly slower than our method, while BLIINDS-II and S3 are the two slowest methods. Currently, MLV is the fastest.

VI. CONCLUSION

Blur is a key determinant in the perception of image quality. Building computational models to evaluate the extents of blur in digital images is thus of great importance. In this paper, we have proposed a novel NR image blur assessment metric, which we call BIBLE for short. It is basically based on the observation that blur distortion changes the shape of an image, and this kind of shape change can be represented using discrete Tchebichef moments, which are effective in shape representation. To this end, we first compute the gradient image, and the energy of the image is computed as the SSM values. The proposed image blur score is then generated by normalizing the moment energy using the block variances with the guidance of a visual saliency model. The block-variance-based normalization is designed to remove the effect of image content, so that the proposed method can generate consistent blur scores across different images. The visual saliency model is incorporated to adapt to the characteristic of human eyes in viewing blurred images.

We have tested the performance of the proposed method on four public image quality databases. The experimental results demonstrate that the proposed method can produce blur scores

highly consistent with subjective evaluation, and it outperforms the state-of-the-art image blur metrics as well as several general-purpose NR-IQA metrics.

REFERENCES

[1] W. S. Lin and C.-C. J. Kuo, "Perceptual visual quality metrics: A survey," *J. Vis. Commun. Image Represent.*, vol. 22, no. 4, pp. 297–312, May 2011.
[2] L. Shao, R. M. Yan, X. L. Li, and Y. Liu, "From heuristic optimization to dictionary learning: A review and comprehensive comparison of image denoising algorithms," *IEEE Trans. Cybern.*, vol. 44, no. 7, pp. 1001–1013, Apr. 2014.
[3] H. C. Zhang, J. C. Yang, Y. N. Zhang, and T. S. Huang, "Image and video restorations via nonlocal kernel regression," *IEEE Trans. Cybern.*, vol. 43, no. 3, pp. 1035–1046, Jun. 2013.
[4] X. Q. Lu, Y. Yuan, and P. K. Yan, "Alternatively constrained dictionary learning for image super resolution," *IEEE Trans. Cybern.*, vol. 44, no. 3, pp. 366–377, Mar. 2014.
[5] H. W. Tian, Y. Zhao, R. R. Ni, L. M. Qin, and X. L. Li, "LDFT-based watermarking resilient to local desynchronization attacks," *IEEE Trans. Cybern.*, vol. 43, no. 6, pp. 2190–2201, Dec. 2013.
[6] D. M. Chandler, "Seven challenges in image quality assessment: Past, present, and future research," *ISRN Signal Process.*, vol. 2013, Nov. 2013, Art. ID 905685.
[7] Z. Wang, A. C. Bovik, H. R. Sheikh, and E. P. Simoncelli, "Image quality assessment: From error visibility to structural similarity," *IEEE Trans. Image Process.*, vol. 13, no. 4, pp. 600–612, Apr. 2004.
[8] H. R. Sheikh and A. C. Bovik, "Image information and visual quality," *IEEE Trans. Image Process.*, vol. 15, no. 2, pp. 430–444, Feb. 2006.
[9] E. C. Larson and D. M. Chandler, "Most apparent distortion: Full-reference image quality assessment and the role of strategy," *J. Electron. Imag.*, vol. 19, no. 1, Mar. 2010, Art. ID 001006.
[10] L. Zhang, L. Zhang, X. Q. Mou, and D. Zhang, "FSIM: A feature similarity index for image quality assessment," *IEEE Trans. Image Process.*, vol. 20, no. 8, pp. 2378–2386, Aug. 2011.
[11] M. Narwaria and W. S. Lin, "SVD-based quality metric for image and video using machine learning," *IEEE Trans. Syst., Man, Cybern. B, Cybern.*, vol. 42, no. 2, pp. 347–364, Apr. 2012.
[12] W. F. Xue, L. Zhang, X. Q. Mou, and A. C. Bovik, "Gradient magnitude similarity deviation: A highly efficient perceptual image quality index," *IEEE Trans. Image Process.*, vol. 23, no. 2, pp. 684–695, Feb. 2014.
[13] D. C. Tao, X. L. Li, W. Lu, and X. B. Gao, "Reduced-reference IQA in contourlet domain," *IEEE Trans. Syst., Man, Cybern. B, Cybern.*, vol. 39, no. 6, pp. 1623–1627, Dec. 2009.
[14] L. Ma, S. N. Li, F. Zhang, and K. N. Ngan, "Reduced-reference image quality assessment using reorganized DCT-based image representation," *IEEE Trans. Multimedia*, vol. 13, no. 4, pp. 824–829, Aug. 2011.
[15] J. J. Wu, W. S. Lin, G. M. Shi, and A. M. Liu, "Reduced-reference image quality assessment with visual information fidelity," *IEEE Trans. Multimedia*, vol. 15, no. 7, pp. 1700–1705, Nov. 2013.
[16] H. H. Chou, L. Y. Hsu, and H. T. Hu, "Turbulent-PSO-based fuzzy image filter with no-reference measures for high-density impulse noise," *IEEE Trans. Cybern.*, vol. 43, no. 1, pp. 296–307, Feb. 2013.
[17] L. D. Li, H. C. Zhu, G. B. Yang, and J. S. Qian, "Referenceless measure of blocking artifacts by Tchebichef kernel analysis," *IEEE Signal Process. Lett.*, vol. 21, no. 1, pp. 122–125, Jan. 2014.

[18] L. D. Li, W. S. Lin, and H. C. Zhu, "Learning structural regularity for evaluating blocking artifacts in JPEG images," *IEEE Signal Process. Lett.*, vol. 21, no. 8, pp. 918–922, Aug. 2014.

[19] H. T. Liu, N. Klomp, and I. Heynderickx, "A no-reference metric for perceived ringing artifacts in images," *IEEE Trans. Circuits Syst. Video Technol.*, vol. 20, no. 4, pp. 529–539, Apr. 2010.

[20] A. K. Moorthy and A. C. Bovik, "A two-step framework for constructing blind image quality indices," *IEEE Signal Process. Lett.*, vol. 17, no. 5, pp. 513–516, May 2010.

[21] M. A. Saad and A. C. Bovik, "Blind image quality assessment: A natural scene statistics approach in the DCT domain," *IEEE Trans. Image Process.*, vol. 21, no. 8, pp. 3339–3352, Aug. 2012.

[22] A. Mittal, A. K. Moorthy, and A. C. Bovik, "No-reference image quality assessment in the spatial domain," *IEEE Trans. Image Process.*, vol. 21, no. 12, pp. 4695–4708, Dec. 2012.

[23] P. Ye, J. Kumar, L. Kang, and D. Doermann, "Unsupervised feature learning framework for no-reference image quality assessment," in *Proc. Int. Conf. Comput. Vis. Pattern Recognit. (CVPR)*, Providence, RI, USA, 2012, pp. 1098–1105.

[24] A. Mittal, A. K. Moorthy, and A. C. Bovik, "Making image quality assessment robust," in *Proc. Asilomar Conf. Signals Syst. Comput.*, Pacific Grove, CA, USA, 2012, pp. 1718–1722.

[25] A. Mittal, R. Soundararajan, and A. C. Bovik, "Making a completely blind image quality analyzer," *IEEE Signal Process. Lett.*, vol. 20, no. 3, pp. 209–212, Mar. 2013.

[26] L. H. He, D. C. Tao, X. L. Li, and X. B. Gao, "Sparse representation for blind image quality assessment," in *Proc. Int. Conf. Comput. Vis. Pattern Recognit. (CVPR)*, Providence, RI, USA, 2012, pp. 1146–1153.

[27] X. B. Gao, F. Gao, D. C. Tao, and X. L. Li, "Universal blind image quality assessment metrics via natural scene statistics and multiple kernel learning," *IEEE Trans. Neural Netw. Learn. Syst.*, vol. 24, no. 12, pp. 2013–2026, Dec. 2013.

[28] L. Kang, P. Ye, Y. Li, and D. Doermann, "Convolutional neural networks for no-reference image quality assessment," in *Proc. Int. Conf. Comput. Vis. Pattern Recognit. (CVPR)*, Columbus, OH, USA, 2014, pp. 1733–1740.

[29] J. Flusser, T. Suk, and B. Zitová, *Moments and Moment Invariants in Pattern Recognition*. New York, NY, USA: Wiley, 2009.

[30] R. Mukundan, S. H. Ong, and P. A. Lee, "Image analysis by Tchebichef moments," *IEEE Trans. Image Process.*, vol. 10, no. 9, pp. 1357–1364, Sep. 2001.

[31] P. T. Yap, R. Paramesran, and S. H. Ong, "Image analysis by Krawtchouk moments," *IEEE Trans. Image Process.*, vol. 12, no. 11, pp. 1367–1377, Nov. 2003.

[32] P. T. Yap, R. Paramesran, and S. H. Ong, "Image analysis using Hahn moments," *IEEE Trans. Pattern Anal. Mach. Intell.*, vol. 29, no. 11, pp. 2057–2062, Nov. 2007.

[33] P. Marziliano, F. Dufaux, S. Winkler, and T. Ebrahimi, "Perceptual blur and ringing metrics: Application to JPEG2000," *Signal Process. Image Commun.*, vol. 19, no. 2, pp. 163–172, Feb. 2004.

[34] S. Q. Wu *et al.*, "Blind blur assessment for vision-based applications," *J. Vis. Commun. Image Represent.*, vol. 20, no. 4, pp. 231–241, May 2009.

[35] R. Ferzli and L. J. Karam, "A no-reference objective image sharpness metric based on the notion of just noticeable blur (JNB)," *IEEE Trans. Image Process.*, vol. 18, no. 4, pp. 717–728, Apr. 2009.

[36] N. D. Narvekar and L. J. Karam, "A no-reference image blur metric based on the cumulative probability of blur detection (CPBD)," *IEEE Trans. Image Process.*, vol. 20, no. 9, pp. 2678–2683, Sep. 2011.

[37] K. Bahrami and A. C. Kot, "A fast approach for no-reference image sharpness assessment based on maximum local variation," *IEEE Signal Process. Lett.*, vol. 21, no. 6, pp. 751–755, Jun. 2014.

[38] P. V. Vu and D. M. Chandler, "A fast wavelet-based algorithm for global and local image sharpness estimation," *IEEE Signal Process. Lett.*, vol. 19, no. 7, pp. 423–426, Jul. 2012.

[39] R. Hassen, Z. Wang, and M. Salama, "Image sharpness assessment based on local phase coherence," *IEEE Trans. Image Process.*, vol. 22, no. 7, pp. 2798–2810, Jul. 2013.

[40] C. T. Vu, T. D. Phan, and D. M. Chandler, "S3: A spectral and spatial measure of local perceived sharpness in natural images," *IEEE Trans. Image Process.*, vol. 21, no. 3, pp. 934–945, Mar. 2012.

[41] E. P. Lyvers, O. R. Mitchell, M. L. Akey, and A. P. Reeves, "Subpixel measurements using a moment-based edge operator," *IEEE Trans. Pattern Anal. Mach. Intell.*, vol. 11, no. 12, pp. 1293–1309, Dec. 1989.

[42] T. J. Bin, L. Ao, J. W. Cui, W. J. Kang, and D. D. Liu, "Subpixel edge location based on orthogonal Fourier-Mellin moments," *Image Vis. Comput.*, vol. 26, no. 4, pp. 563–569, Apr. 2008.

[43] C. Y. Wee, R. Paramesran, R. Mukundan, and X. D. Jiang, "Image quality assessment by discrete orthogonal moments," *Pattern Recognit.*, vol. 43, no. 12, pp. 4055–4068, Dec. 2010.

[44] K. H. Thung, R. Paramesran, and C. L. Lim, "Content-based image quality metric using similarity measure of moment vectors," *Pattern Recognit.*, vol. 45, no. 6, pp. 2193–2204, Jun. 2012.

[45] R. Mukundan, "Some computational aspects of discrete orthonormal moments," *IEEE Trans. Image Process.*, vol. 13, no. 8, pp. 1055–1059, Aug. 2004.

[46] L. M. Zhang and W. S. Lin, *Modeling Selective Visual Attention: Techniques and Applications*. Singapore: Wiley, 2013.

[47] L. Zhang, Z. Y. Gu, and H. Y. Li, "SDSP: A novel saliency detection method by combining simple priors," in *Proc. IEEE Conf. Image Process. (ICIP)*, Paris, France, 2013, pp. 171–175.

[48] L. Zhang, Y. Shen, and H. Y. Li, "VSI: A visual saliency induced index for perceptual image quality assessment," *IEEE Trans. Image Process.*, vol. 23, no. 10, pp. 4270–4281, Oct. 2014.

[49] H. R. Sheikh, M. F. Sabir, and A. C. Bovik, "A statistical evaluation of recent full reference image quality assessment algorithms," *IEEE Trans. Image Process.*, vol. 15, no. 11, pp. 3440–3451, Nov. 2006.

[50] N. Ponomarenko *et al.*, "TID2008-A database for evaluation of full-reference visual quality assessment metrics," *Adv. Modern Radioelectron.*, vol. 10, no. 4, pp. 30–45, 2009.

[51] N. Ponomarenko *et al.*, "Color image database TID2013: Peculiarities and preliminary results," in *Proc. Eur. Workshop Vis. Inf. Process.*, 2013, pp. 106–111.

[52] (Aug. 2003). *Final Report From the Video Quality Experts Group on the Validation of Objective Models of Video Quality Assessment, Phase II.* [Online]. Available: http://www.vqeg.org

[53] Z. Wang and Q. Li, "Information content weighting for perceptual image quality assessment," *IEEE Trans. Image Process.*, vol. 20, no. 5, pp. 1185–1198, May 2010.
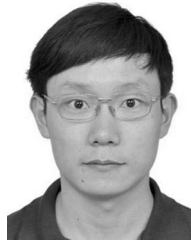
Leida Li (M'14) received the B.S. and Ph.D. degrees from Xidian University, Xi'an, China, in 2004 and 2009, respectively.

In 2008, he was a visiting Ph.D. student at the Department of Electronic Engineering, National Kaohsiung University of Applied Sciences, Kaohsiung, Taiwan, for five months. From 2014 to 2015, he was a Visiting Research Fellow at the School of Electrical and Electronic Engineering, Nanyang Technological University, Singapore. He is currently an Associate Professor with the School of Information and Electrical Engineering, China University of Mining and Technology, Xuzhou, China. His current research interests include multimedia quality assessment, information hiding, and image forensics.

Weisi Lin (M'92–SM'98) received the B.S. and M.S. degrees from Zhongshan University, Guangzhou, China, in 1982 and 1985, respectively, and the Ph.D. degree from Kings College, London University, London, U.K., in 1992.

He was the Laboratory Head of Visual Processing and the Acting Department Manager of Media Processing at the Institute for Infocomm Research, Singapore. He is currently an Associate Professor with the School of Computer Engineering, Nanyang Technological University, Singapore. His current research interests include image processing, perceptual modeling, video compression, multimedia communication, and computer vision. He has published over 200 refereed papers in international journals and conferences.

Dr. Lin served as an Associate Editor for the IEEE TRANSACTIONS ON MULTIMEDIA. He is currently on the editorial boards of the IEEE SIGNAL PROCESSING LETTERS and the *Journal of Visual Communication and Image Representation*. He also served as the Lead Guest Editor for a Special Issue on Perceptual Signal Processing and the IEEE JOURNAL OF SELECTED TOPICS IN SIGNAL PROCESSING 2012. He was the Co-Chair of the IEEE Multimedia Communications Technical Committee Special Interest Group on Quality of Experience. He was a Distinguished Lecturer of Asia-Pacific Signal and Information Processing Association from 2012 to 2013. He was the Lead Technical Program Chair of the Pacific-Rim Conference on Multimedia 2012 and a Technical Program Chair of the IEEE International Conference on Multimedia and Expo 2013. He is a Chartered Engineer (U.K.), a fellow of the Institution of Engineering Technology, and an Honorary Fellow, Singapore Institute of Engineering Technologists.

Xuesong Wang received the Ph.D. degree from the China University of Mining and Technology, Xuzhou, China, in 2002.

She is currently a Professor with the School of Information and Electrical Engineering, China University of Mining and Technology. Her current research interests include machine learning, bioinformatics, and artificial intelligence.

Dr. Wang was the recipient of the New Century Excellent Talents in University from the Ministry of Education of China in 2008.

Gaobo Yang received the Ph.D. degree in communication and information system from Shanghai University, Shanghai, China, in 2004.

He is currently a Professor with Hunan University, Changsha, China. His current research interests include image and video signal processing and digital media forensics.

Dr. Yang was the recipient of the New Century Excellent Talents in University Award from the Ministry of Education of China in 2011. He is a key member of Hunan Provincial Key Laboratory of Networks and Information Security.

Khosro Bahrami (S'10) received the B.Sc. and M.Sc. degrees in computer engineering from Shiraz University, Shiraz, Iran, and the Sharif University of Technology, Tehran, Iran, in 2000 and 2002, respectively. He is currently pursuing the Ph.D. degree from the School of Electrical and Electronic Engineering, Nanyang Technological University, Singapore.

His current research interests include image quality assessment, image enhancement, computer vision, and image forensics.

Mr. Bahrami served as a reviewer for the IEEE TRANSACTIONS ON CYBERNETICS, the IEEE TRANSACTIONS ON IMAGE PROCESSING, and the IEEE TRANSACTIONS ON INFORMATION FORENSICS AND SECURITY.

Alex C. Kot (S'85–M'89–SM'98–F'06) received the Ph.D. degree from the University of Rhode Island, RI, USA, in 1989.

He has been with Nanyang Technological University, Singapore, since 1991. He was the Head of the Division of Information Engineering, for eight years, and an Associate Chair/Research and the Vice Dean for Research at the School of Electrical and Electronic Engineering, Nanyang Technological University. He is currently a Professor and an Associate Dean with the College of Engineering and the Director of Rapid-Rich Object Seearch Laboratory, Nanyang Technological University. He has published extensively in the areas of signal processing for communication, biometrics, data-hiding, image forensics, and information security and co-authored several conferences such as International Conference on Pattern Recognition (ICPR), IEEE International Workshop on Information Forensics and Security (WIFS), International Conference on Electronic Commerce (ICEC), and International Workshop on Digital-Forensics and Watermarking (IWDW).

Dr. Kot was the recipient of the Best Teacher of the Year Award and several Best Paper Awards including ICPR, IEEE WIFS, ICEC, and IWDW. He served as an Associate Editor for the IEEE TRANSACTIONS ON SIGNAL PROCESSING, the IEEE TRANSACTIONS ON MULTIMEDIA, the IEEE SIGNAL PROCESSING LETTERS, the IEEE SIGNAL PROCESSING MAGAZINE, the IEEE JOURNAL OF SELECTED TOPICS IN SIGNAL PROCESSING, the IEEE TRANSACTIONS ON CIRCUITS AND SYSTEMS FOR VIDEO TECHNOLOGY, the IEEE TRANSACTIONS ON CIRCUITS AND SYSTEMS PART I AND PART II, and the IEEE TRANSACTIONS ON IMAGE PROCESSING. He also served as a Guest Editor for Special Issues on the IEEE TRANSACTIONS ON CSVT and JASP. He is currently an Associate Editor of the IEEE TRANSACTIONS ON INFORMATION FORENSICS AND SECURITY. He is also an Editor of the *EURASIP Journal on Advanced in Signal Processing*. He has served on the IEEE SP Society in various capacities such as the General Co-Chair for the 2004 IEEE International Conference on Image Processing, the IEEE Signal Processing Society (SPS) Distinguished Lecturer Program Coordinator and the Chapters Chair for IEEE Signal Processing Chapters worldwide. He currently serves as the Vice-President for the IEEE Signal Processing Society. He is an IEEE SPS Distinguished Lecturer and a fellow of the Academy of Engineering, Singapore, a Fellow of IEEE and a Fellow of IES.